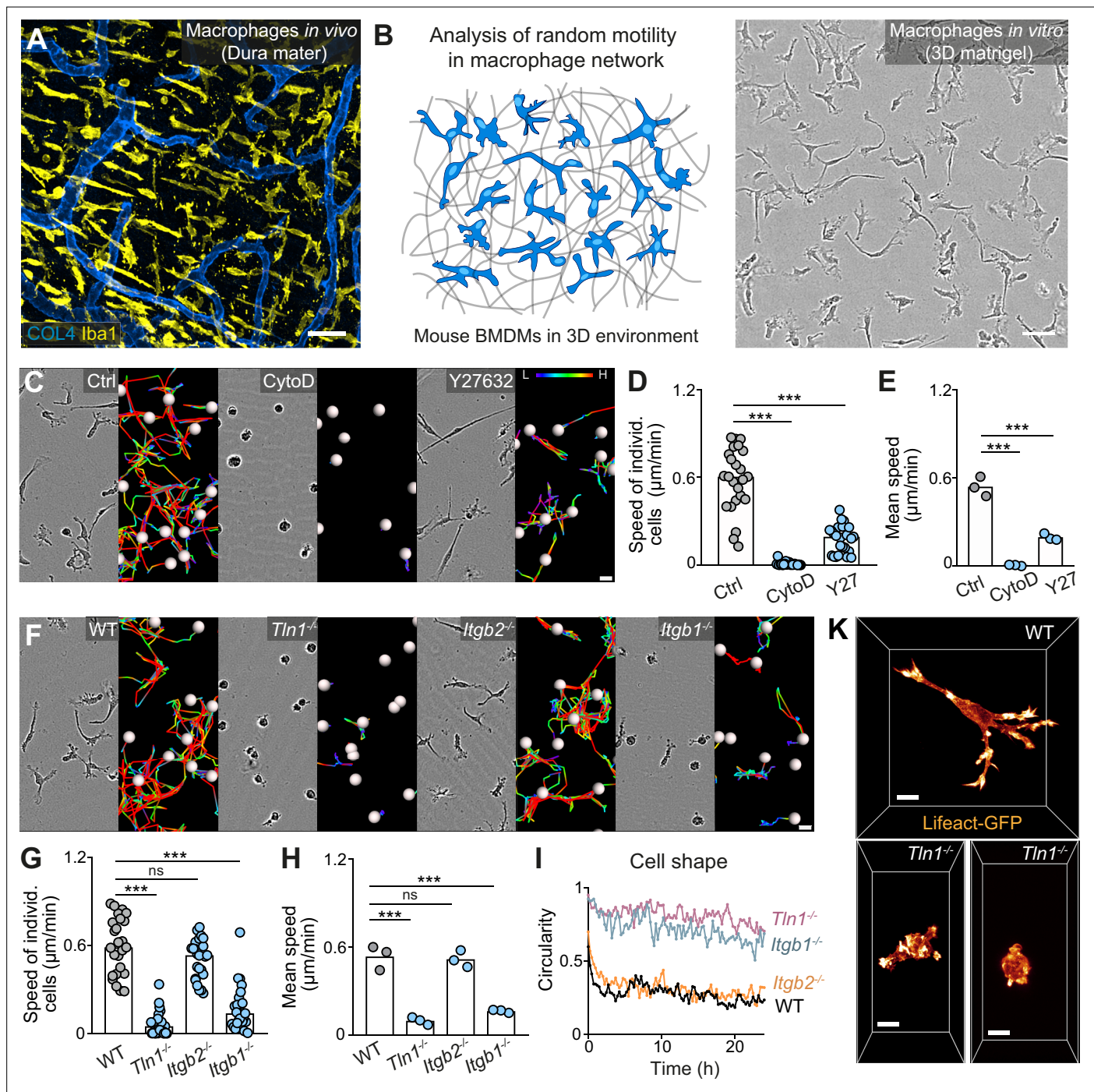


---

## Figures and figure supplements

Macrophage network dynamics depend on haptokinesis for optimal local surveillance

**Neil Paterson and Tim Lämmermann**



**Figure 1.** Haptokinetic random motility of macrophages in three-dimensional (3D) matrices. **(A)** Representative macrophage network in adult mouse tissue. Immunofluorescence staining of a dura mater whole mount preparation, showing macrophages (yellow) and blood vasculature (blue). COL4: collagen IV. **(B)** Scheme (left) and brightfield image (right) for studying macrophage network dynamics in 3D in vitro matrices. **(C–E)** Analysis of bone marrow-derived macrophage (BMDM) random motility in the presence of cytochalasin D (CytoD) or Y27632. **(C)** Representative cell morphologies (brightfield microscopy) and pseudo-colored tracks (displacement delta length: L(low) = 0, H(high) = 15) over 24 hr. **(D)** Individual cell speeds from one independent experiment (dots represent randomly chosen cells per condition, N = 25), and **(E)** mean speed values calculated from three biological replicates (n = 3). **(F–H)** Analysis of BMDM random motility upon genetic interference with integrin functionality, including **(F)** cell morphologies and tracks over 24 hr, **(G)** individual cell speeds from one independent experiment (N = 25), and **(H)** mean speed values calculated from three biological replicates (n = 3). **(I)** Graphical analysis of cell shape at 15 min time intervals over 24 hr for integrin-mutant BMDMs. Dots are mean values of N = 5 randomly chosen cells per genotype. A circularity value of 1 equals a perfectly circular cell. **(K)** Confocal live-cell microscopy of Lifeact-GFP expressing WT or *Tln1*<sup>-/-</sup> BMDMs in 3D matrigel. Bars in graphs: median (**D**, **G**), mean (**E**, **H**). Statistical tests: \*\*\*p ≤ 0.001, Dunn's multiple comparison (post hoc).

Figure 1 continued on next page

Figure 1 continued

Kruskal-Wallis test) (**D**, **G**); \*\*\* $p \leq 0.001$ , Dunnett's multiple comparison (post hoc analysis of variance [ANOVA]) (**E**, **H**). Scale bars: 50  $\mu\text{m}$  (**A**, **B**), 10  $\mu\text{m}$  (**K**), 20  $\mu\text{m}$  (**C**, **F**).

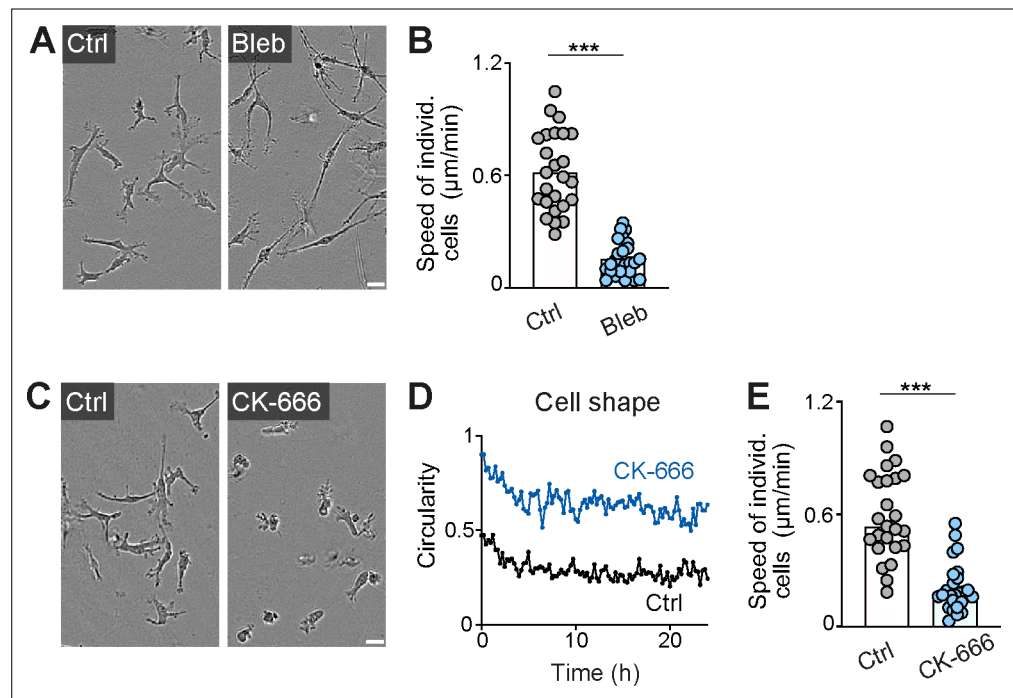


**Figure 1—figure supplement 1.** Actomyosin contraction and dendritic actin networks regulate random motility of macrophages in three-dimensional (3D) matrices. **(A, B)** Analysis of bone marrow-derived macrophage (BMDM) random motility in the presence of blebbistatin in 3D matrigel. **(A)** Representative cell morphologies (brightfield microscopy), **(B)** individual cell speeds from one independent experiment (dots represent randomly chosen cells per condition, N = 25). Bars display the mean; \*\*\*p ≤ 0.001, t test. **(C–E)** Analysis of BMDM random motility in the presence of CK-666 in 3D matrigel. **(C)** Representative cell morphologies (brightfield microscopy), **(D)** graphical analysis of cell shape at 15 min time intervals over 24 hr. Dots are mean values of N = 5 randomly chosen cells per genotype. A circularity value of 1 equals a perfectly circular cell, **(E)** individual cell speeds from one independent experiment (dots represent randomly chosen cells per condition, N = 25). Bars display the median; \*\*\*p ≤ 0.001, U test. Scale bars: 20 μm.



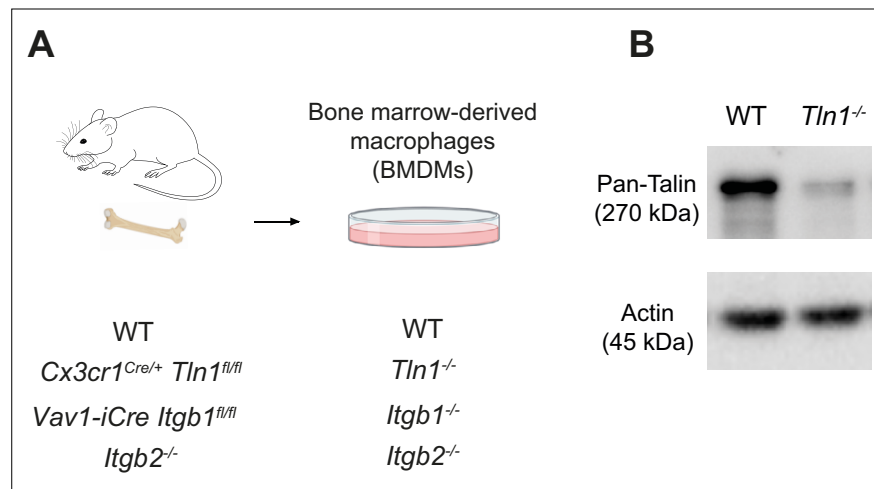


**Figure 1—figure supplement 2.** Characterization of mouse bone marrow-derived macrophages (BMDMs) with impaired integrin functionality. **(A)** Scheme for the generation of BMDMs from conditional and constitutive knockout mouse models to obtain BMDMs depleted for talin-1 (*Tln1*<sup>-/-</sup>) or cell surface integrins from the  $\beta$ 1 family (*Itgb1*<sup>-/-</sup>) or  $\beta$ 2 family (*Itgb2*<sup>-/-</sup>). **(B)** The efficiency of conditional talin-1 knockout was confirmed by immunoblot analysis (by using a pan-talin antibody recognizing talin-1 and talin-2). Cell lysates were generated from WT and *Tln1*<sup>-/-</sup> BMDMs. Actin was used as loading control.

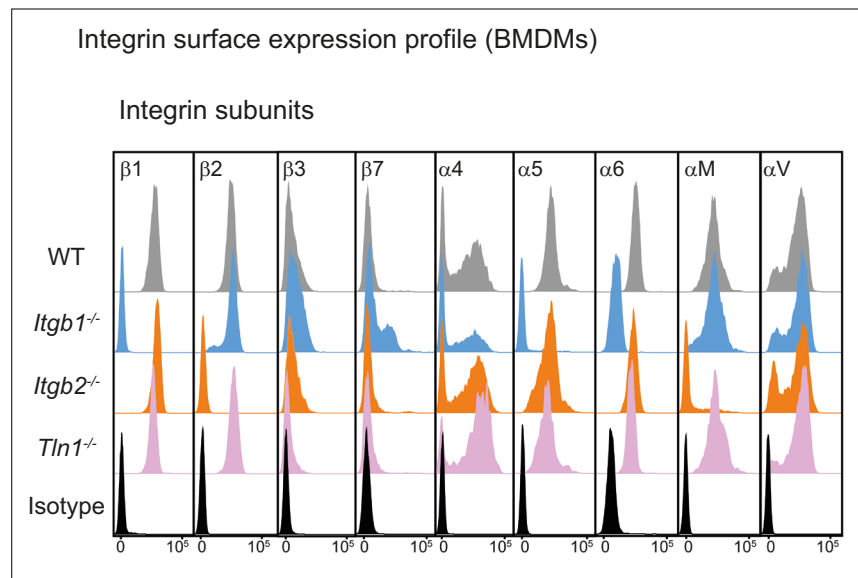


**Figure 1—figure supplement 3.** Characterization of mouse bone marrow-derived macrophages (BMDMs) with impaired integrin functionality. Flow cytometry analysis of integrin subunits expressed on the surface of WT, *Itgb1*<sup>-/-</sup>, *Itgb2*<sup>-/-</sup>, and *Tln1*<sup>-/-</sup> BMDMs.  $\beta 1$  integrin depletion leads to loss of fibronectin-binding  $\alpha 5\beta 1$  and laminin-binding  $\alpha 6\beta 1$  integrins from the cell surface of *Itgb1*<sup>-/-</sup> macrophages. A pool of the  $\alpha 4$  subunit remains retained on the cell surface in combination with an upregulation of the corresponding  $\beta 7$  subunit. This switch from  $\alpha 4\beta 1$  to  $\alpha 4\beta 7$  heterodimers is a well-documented phenomenon for *Itgb1*<sup>-/-</sup> leukocytes.  $\beta 2$  integrin deficiency leads to loss of the  $\alpha M$  subunit (CD11b) and thus  $\alpha M\beta 2$  (Mac-1, CR3) from the macrophage surface. Talin depletion in BMDMs leaves the cell surface integrin expression profile unchanged.

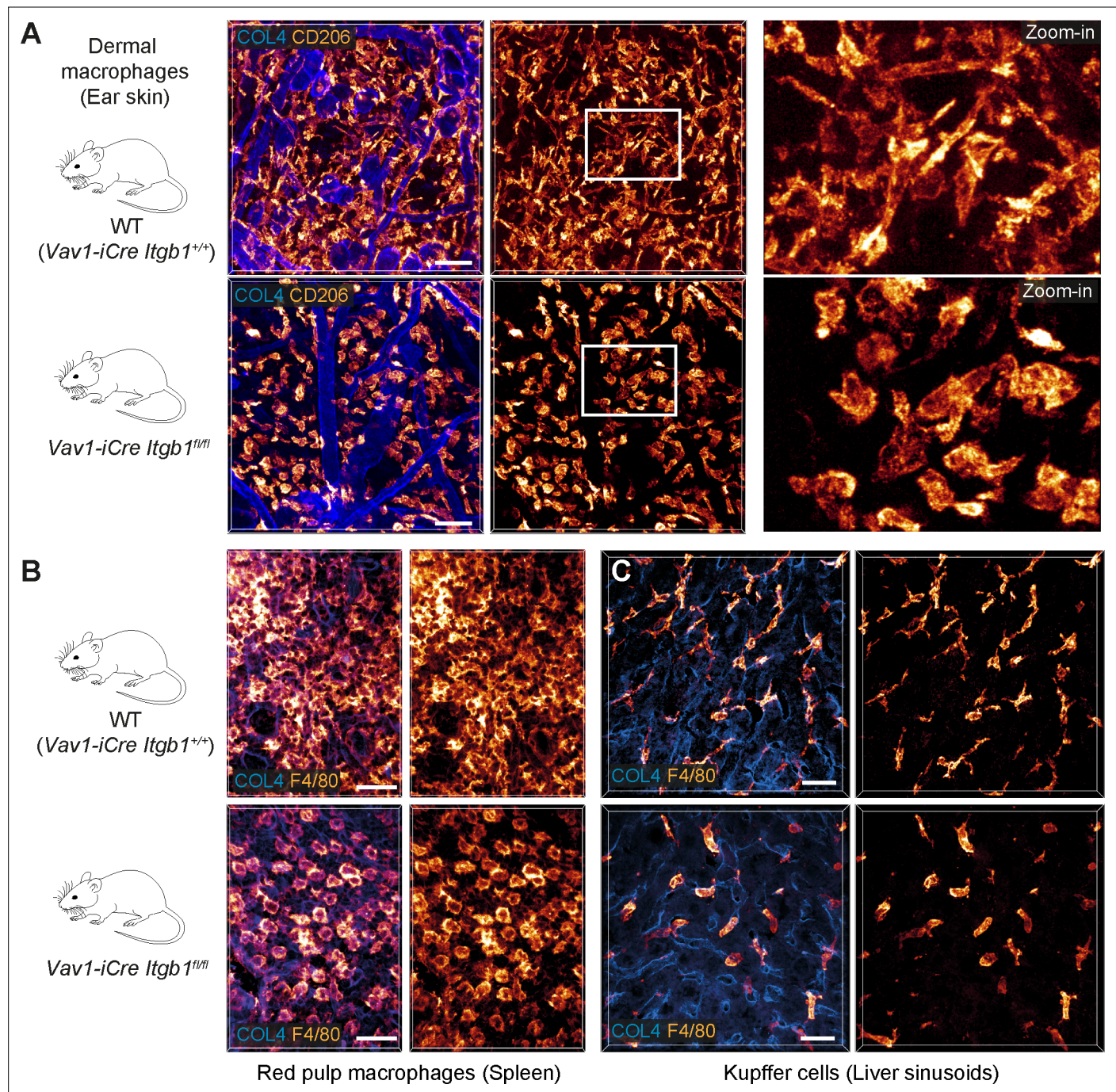


**Figure 2.**  $\beta 1$  integrins define the mesenchymal shape of macrophages in mouse tissues. (A–C) Comparative analysis of ear skin dermis (A), spleen (B) and liver (C) tissues of adult *Vav1-iCre<sup>+/+</sup> Itgb1<sup>fl/fl</sup>* mice and littermate controls. Endogenous macrophage subsets were detected with immunostainings against CD206 (A) and F4/80 (B, C) and fluorescence signal intensities displayed as glow heatmap color. Collagen IV (COL4)-expressing basement membrane (A, C) or reticular network (B) structures are also displayed (blue). All images are projections of several confocal z-planes. Scale bars: 50  $\mu$ m (A), 30  $\mu$ m (B, C).



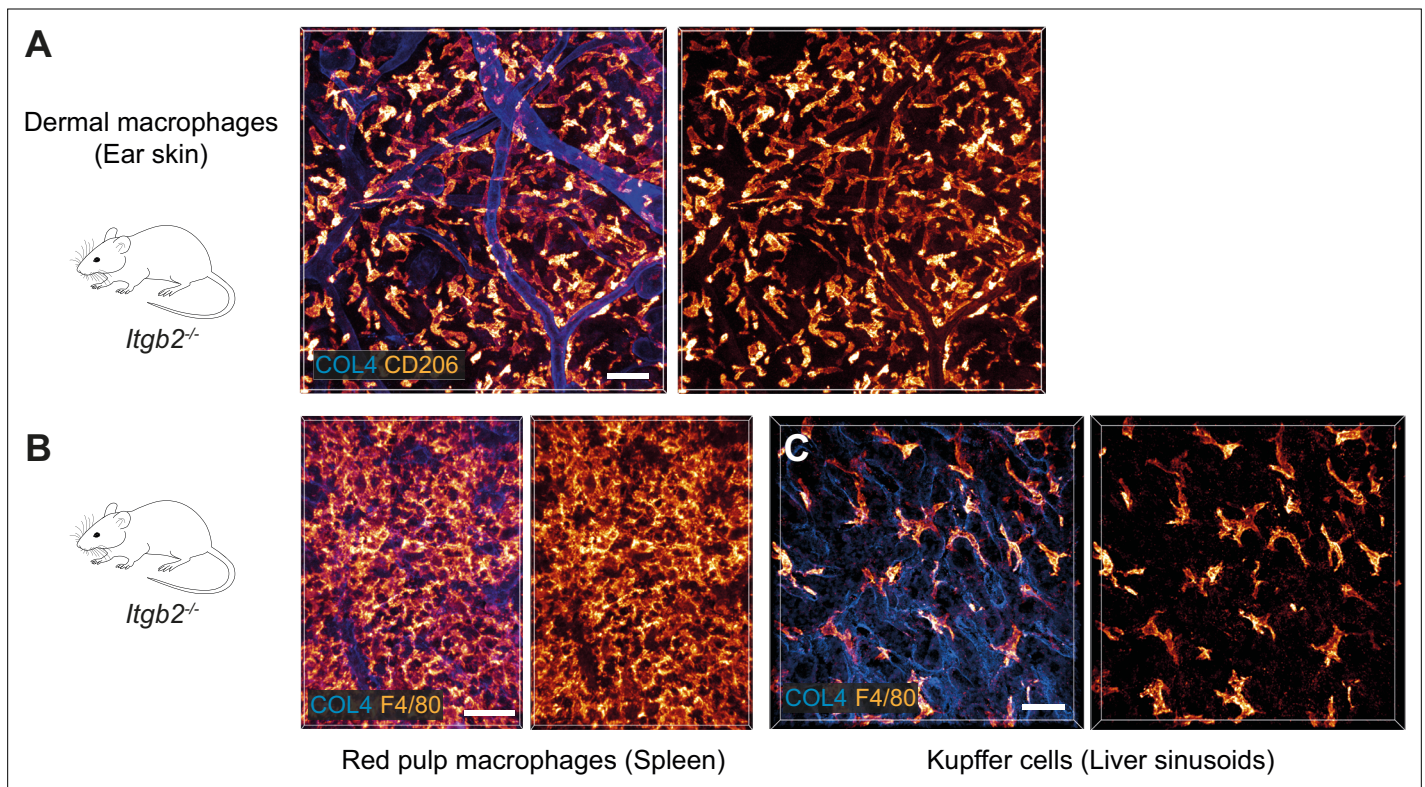


**Figure 2—figure supplement 1.**  $\beta 2$  integrins do not contribute to the mesenchymal shape of macrophages in mouse tissues. (A–C) Immunofluorescence analysis of ear skin dermis (A), spleen (B) and liver (C) tissues of adult *Itgb2<sup>-/-</sup>* mice. Endogenous macrophage subsets were detected with immuno-stainings against CD206 (A) and F4/80 (B,C) and fluorescence signal intensities displayed as glow heatmap color. Collagen IV (COL4)-expressing basement membrane (A, C) or reticular network (B) structures are also displayed (blue). All images are projections of several confocal z-planes. Scale bars: 50  $\mu$ m (A), 30  $\mu$ m (B, C).

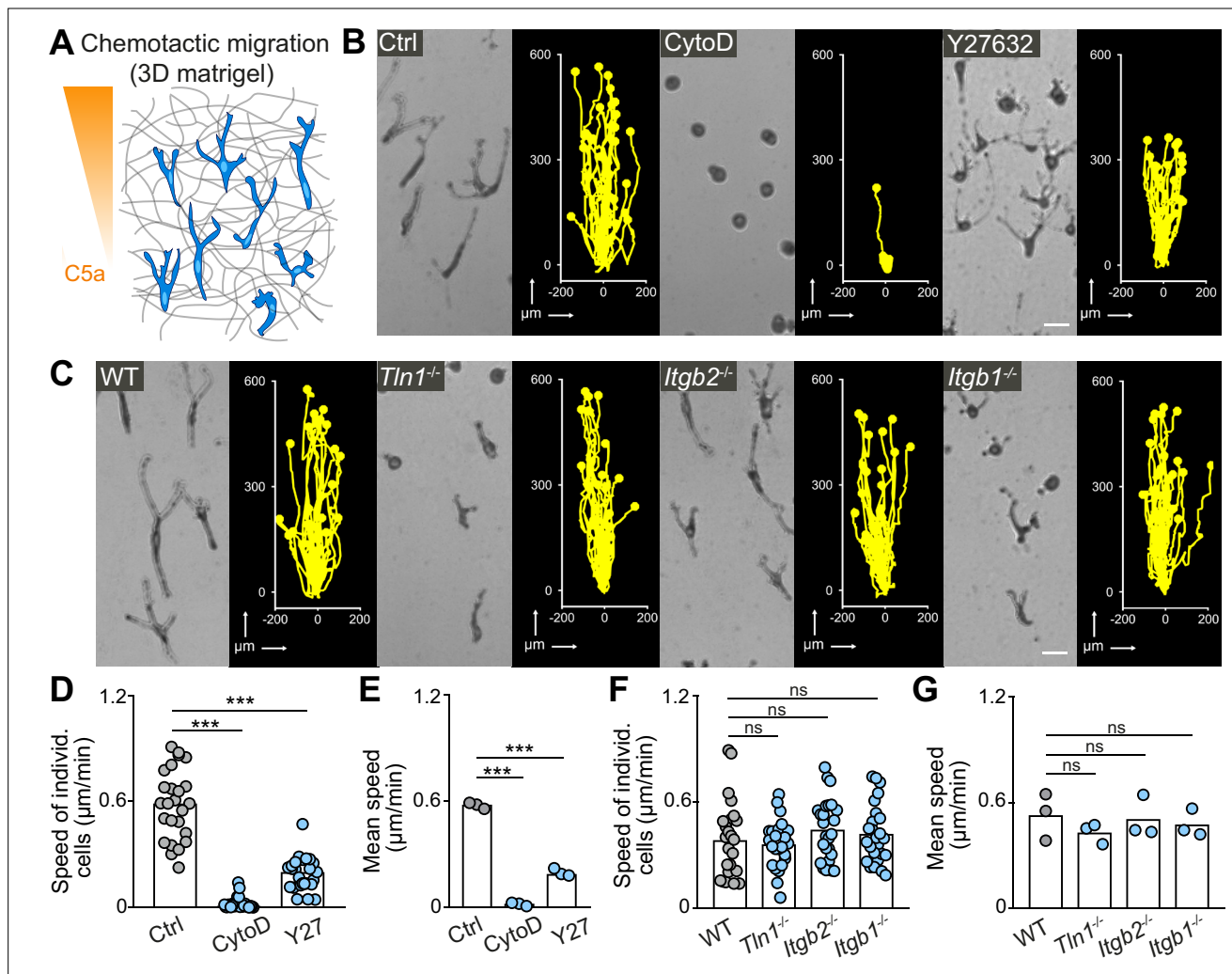


**Figure 3.** Integrin-independent three-dimensional (3D) macrophage movement during chemotactic responses. **(A)** Scheme for studying chemotactic macrophage migration toward C5a gradients in 3D in vitro matrices. **(B, C)** Representative cell morphologies (brightfield microscopy) and tracks over 24 hr of chemotaxing bone marrow-derived macrophages (BMDMs) **(B)** in the presence of cytochalasin D (CytoD) and Y27632, and **(C)** upon genetic interference with integrin functionality. Scale bars: 25 μm. **(D–G)** Analysis of BMDM chemotactic migration, including **(D,F)** individual cell speeds from one independent experiment (dots represent randomly chosen cells per condition, N = 25), and **(E,G)** mean speed values of three biological replicates (n = 3). Bars in graphs: median **(D–F)**, mean **(E–G)**. Statistical tests: \*\*\*p ≤ 0.001, Dunn's multiple comparison (post hoc Kruskal-Wallis test) **(D)**; \*\*\*p ≤ 0.001, Dunnett's multiple comparison (post hoc analysis of variance [ANOVA]) **(E–G)**.

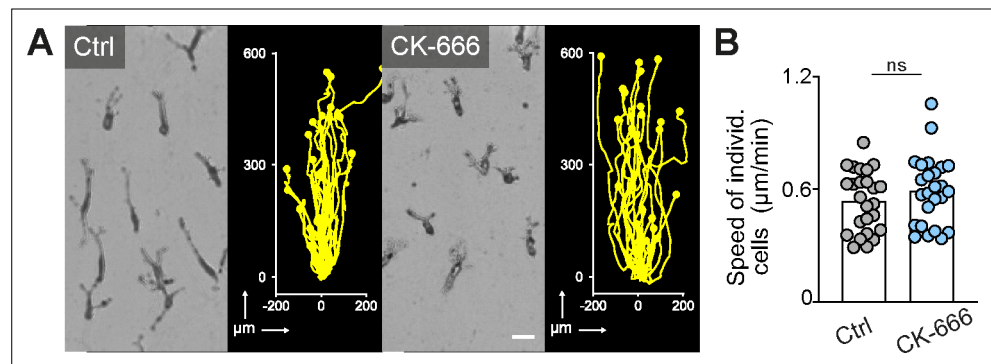


**Figure 3—figure supplement 1.** Arp2/3 complex-mediated dendritic actin networks are dispensable for macrophage chemotaxis in three-dimensional (3D) matrigel. **(A)** Representative cell morphologies (brightfield microscopy) and tracks over 24 hr of bone marrow-derived macrophages (BMDMs) following a C5a gradient in matrigel in the presence of CK-666. Scale bar: 25  $\mu\text{m}$ . **(B)** Analysis of BMDM chemotactic migration, individual cell speeds from one independent experiment (dots represent randomly chosen cells per condition,  $N = 25$ ). Bars display the mean; ns: non-significant,  $t$  test.



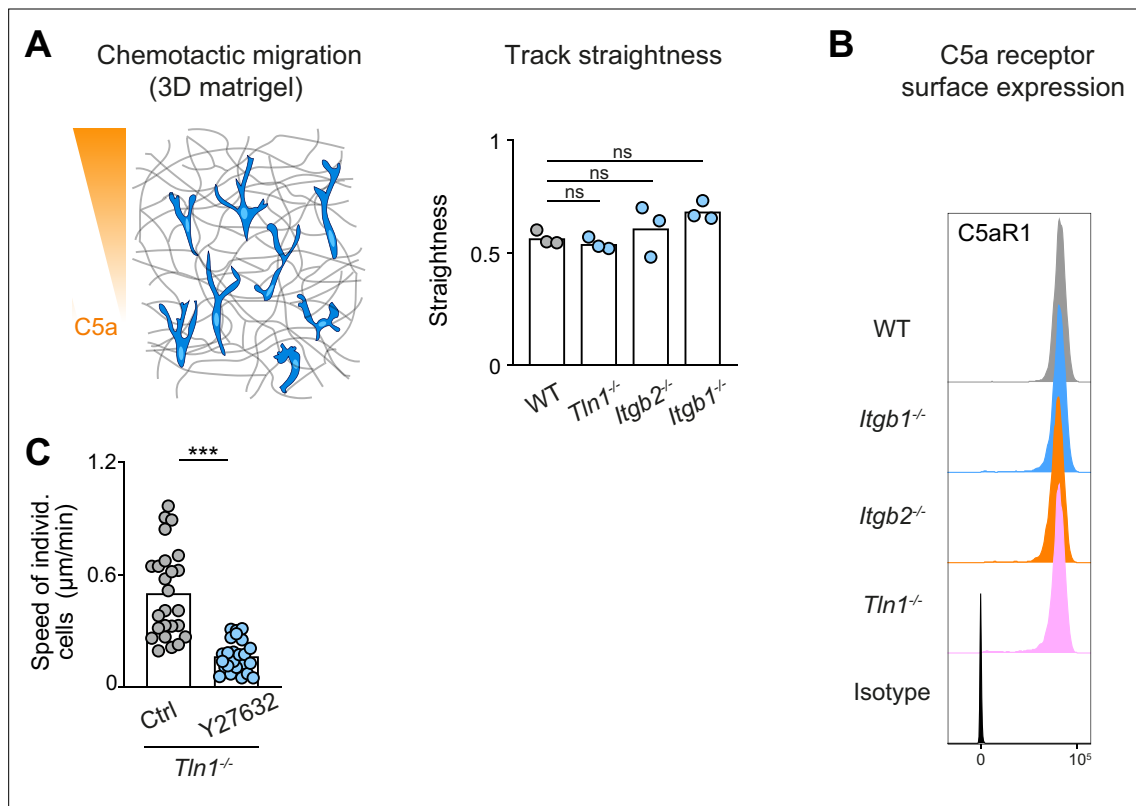


**Figure 3—figure supplement 2.** Track straightness and C5aR1 expression are unaltered in chemotaxing bone marrow-derived macrophages (BMDMs) with impaired integrin functionality. **(A)** Analysis of track straightness during BMDM chemotactic migration toward C5a gradients. Mean speed values were calculated from three biological replicates (n = 3). In each biological replicate N = 25 cells were tracked and analyzed. Bars in graph display the mean; ns: non-significant, Dunnett's multiple comparison (post hoc analysis of variance [ANOVA]). **(B)** Flow cytometry analysis of C5aR1 cell surface expression on WT, *Itgb1*<sup>-/-</sup>, *Itgb2*<sup>-/-</sup>, and *Tln1*<sup>-/-</sup> BMDMs. C5aR1 acts as the major chemotactic receptor for the chemoattractant C5a. **(C)** Analysis of *Tln1*<sup>-/-</sup> BMDM chemotactic migration toward a C5a gradient in three-dimensional (3D) matrigel in the presence of Y27632, individual cell speeds from one independent experiment (dots represent randomly chosen cells per condition, N = 25). Bars display the mean; \*\*\*p ≤ 0.001, t test.

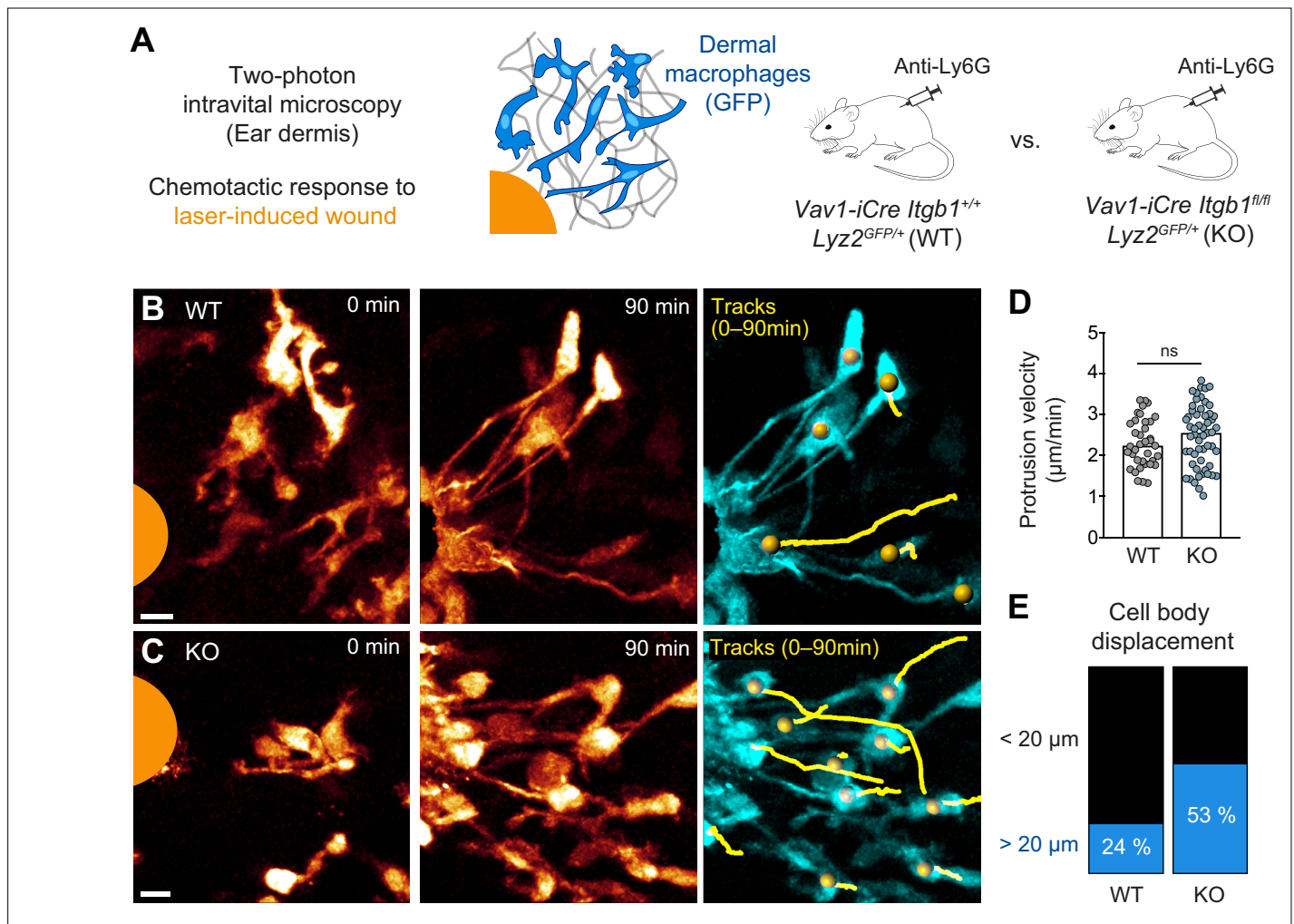


**Figure 4.** Amoeboid-like macrophages still perform chemotactic migration in mouse tissue. **(A)** Scheme for studying the chemotactic response of dermal macrophages to laser-induced tissue injury in mouse ear skin. Two-photon intravital microscopy (2P-IVM) was performed on *Vav1-iCre Itgb1<sup>fl/fl</sup> Lyz2<sup>GFP/+</sup>* and littermate control mice. Mice were treated with Anti-Ly6G antibody to deplete neutrophils and avoid their presence in imaging field of views. **(B, C)** 2P-IVM images of GFP-expressing dermal macrophages in WT mice **(B)** and conditional *Itgb1*-deficient mice **(C)** at the onset of the wound response and 90 min later. GFP signal is displayed as glow heatmap color. Cell body displacements are shown as yellow tracks. Scale bars: 10  $\mu\text{m}$ . **(D)** Velocity analysis of macrophage protrusions moving toward the tissue lesion. Each dot represents one protrusion (WT: N = 37; KO: N = 55). Values are pooled from n = 3 (WT) and n = 4 (KO) mice; ns: non-significant, U test. Bars are median. **(E)** Cell bodies of responding macrophages were tracked and categorized according to displacement (WT: N = 34; KO: N = 55). Values are pooled from n = 3 (WT) and n = 4 (KO) mice.

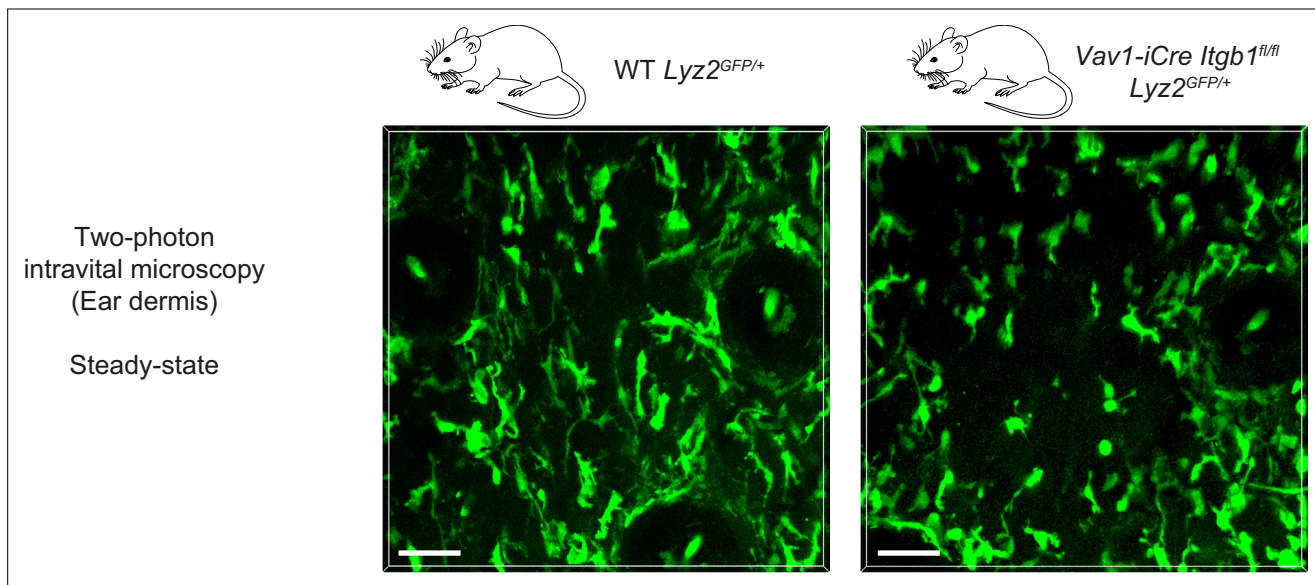


**Figure 4—figure supplement 1.** Two-photon intravital microscopy of macrophage shapes in unchallenged mouse skin. Two-photon intravital microscopy of the dermal compartment in unchallenged ear skin reveals mesenchymal shapes with multiple elongated protrusions in GFP-positive macrophages of WT *Lyz2*<sup>GFP/+</sup> mice. In contrast, the majority of GFP-positive macrophages in the dermis of *Vav1-iCre Itgb1*<sup>fl/fl</sup> *Lyz2*<sup>GFP/+</sup> mice showed more amoeboid-like morphologies and less pronounced cell protrusions. Scale bars: 50  $\mu$ m.

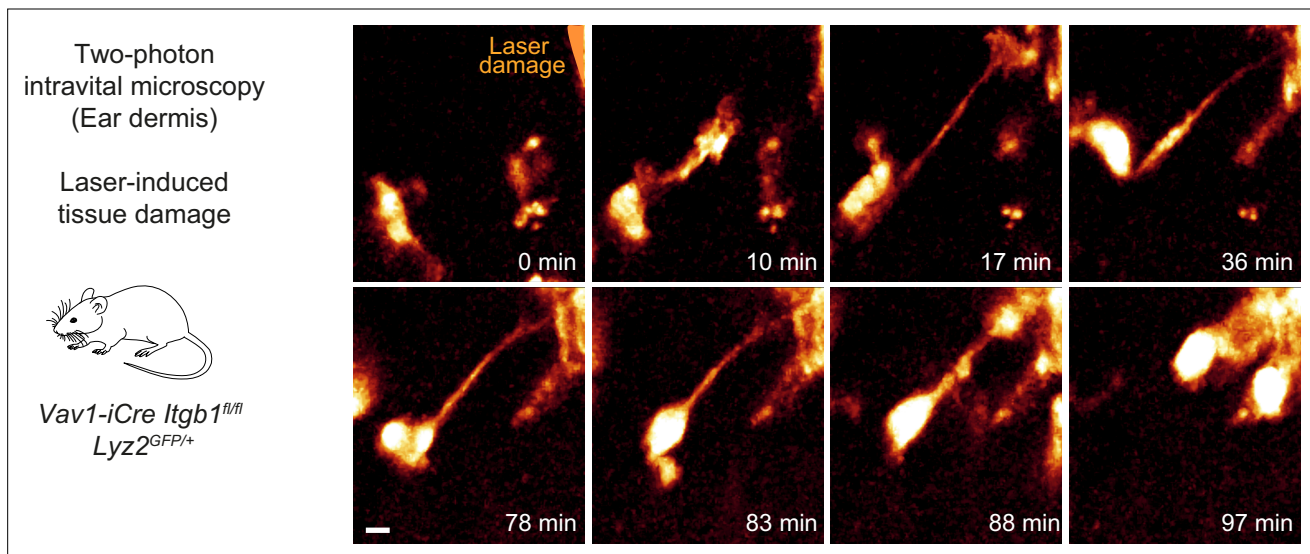


**Figure 4—figure supplement 2.** *Itgb1*-deficient dermal macrophages perform chemotactic migration in mouse skin tissue. Close-up view and time sequence of an *Itgb1*-deficient macrophage that chemotactically responds to a laser-induced tissue lesion in the mouse dermis. Despite lack of  $\beta 1$  integrins and loss of mesenchymal cell shape, these cells form directed protrusions and displace their cell bodies toward the wound site. Scale bar: 5  $\mu$ m.



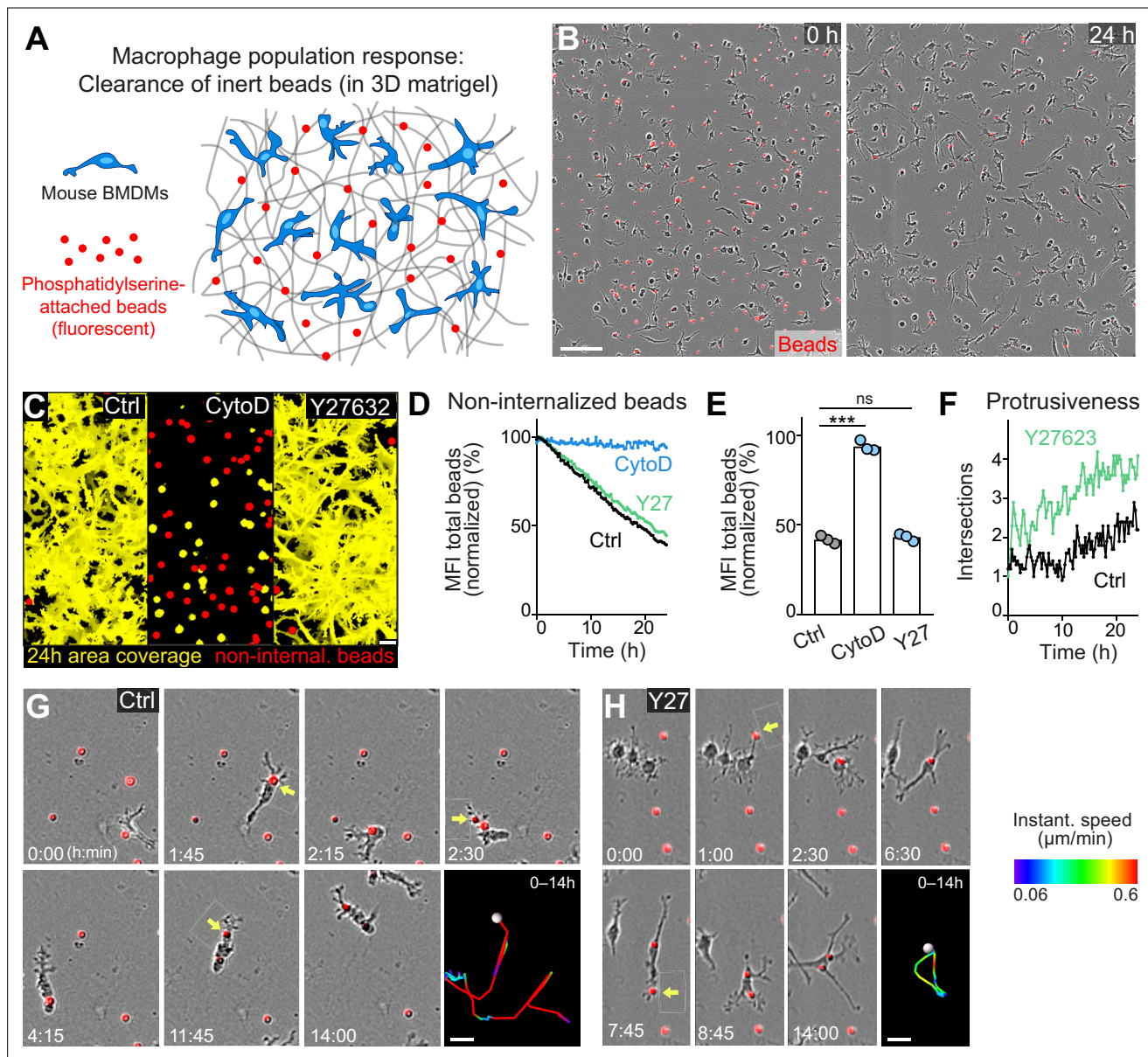


**Figure 5.** Movement and protrusiveness as two sampling strategies for bead removal by macrophage networks. **(A)** Scheme for studying macrophage network surveillance in three-dimensional (3D) in vitro matrices. **(B)** Images of start (0 hr) and endpoint (24 hr) of bead removal by a population of WT bone marrow-derived macrophages (BMDMs) (unstained). Extracellular, fluorescent beads with surface-attached phosphatidylserine (red, 0 hr) were ingested by BMDMs over time. The image shows a quarter of the total imaging field of view. **(C–E)** Analysis of BMDM network sampling activity in the presence of cytochalasin D (CytoD) or Y27632, including **(C)** time projections of macrophage shapes over 24 hr, displayed as total area coverage (yellow) in relation to non-internalized beads (red). Bead sampling by macrophages was measured as mean fluorescence intensity (MFI) decline of bead fluorescence in 15 min intervals over time, presented as **(D)** time-course analysis from one independent experiment (dots in curves are mean values from  $N = 4$ –5 technical replicates (separate wells of matrigel)), and as **(E)** 24 hr-mean-values calculated from three biological replicates ( $n = 3$  per genotype). **(F)** Cell protrusiveness of WT and Y27632-treated BMDMs was determined by Sholl analysis for  $N = 10$  randomly chosen cells and presented as mean values at 15 min time intervals over 24 hr. **(G, H)** Time sequences of individual control **(G)** and Y27632-treated (Y27) **(H)** BMDMs, correlating bead sampling and migratory activity. Yellow arrows highlight bead uptake events. Cell tracks over 14 hr are pseudo-colored for instantaneous speed values. All bar graphs display the mean; \*\*\* $p \leq 0.001$ , ns: non-significant; Dunnett's multiple comparison (post hoc analysis of variance [ANOVA]). Scale bars: 100  $\mu\text{m}$  **(B)**, 40  $\mu\text{m}$  **(C)**, 20  $\mu\text{m}$  **(G, H)**.

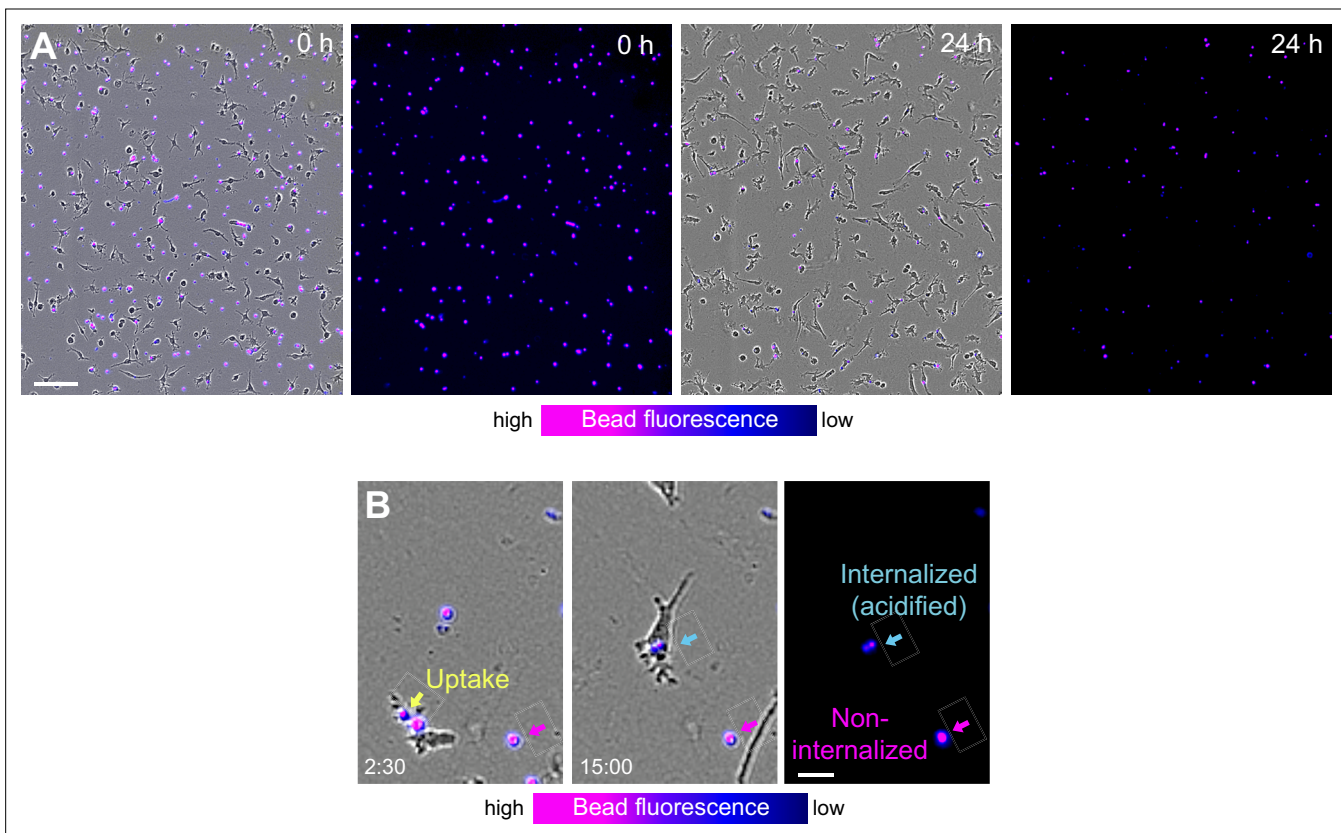


**Figure 5—figure supplement 1.** Removal of fluorescent phosphatidylserine-attached beads by macrophage networks and individual macrophages. **(A)** Live-cell imaging snapshots showing the start (0 hr) and endpoint (24 hr) of bead removal by a population of WT bone marrow-derived macrophages (BMDMs) (unstained). Fluorescent phosphatidylserine-attached beads were extracellular (red, 0 hr) and fluorescence signal displayed as purple-blue heatmap color. At the onset of the experiment, most beads were extracellular and showed high fluorescence signal. After 24 hr, the majority of beads was internalized by macrophages and showed low fluorescence signal. Scale bars: 100  $\mu$ m. **(B)** Live-cell imaging and close-up view of an individual WT BMDM that takes up a fluorescent bead at 2 hr 30 min (yellow arrow). Approximately 12 hr later this internalized bead (light blue arrow) showed reduced signal due to fluorescence quenching in the acidic phagolysosomal compartment of the macrophage. In contrast, non-internalized beads (purple arrow) maintain the fluorescence signal over time. Scale bar: 20  $\mu$ m.



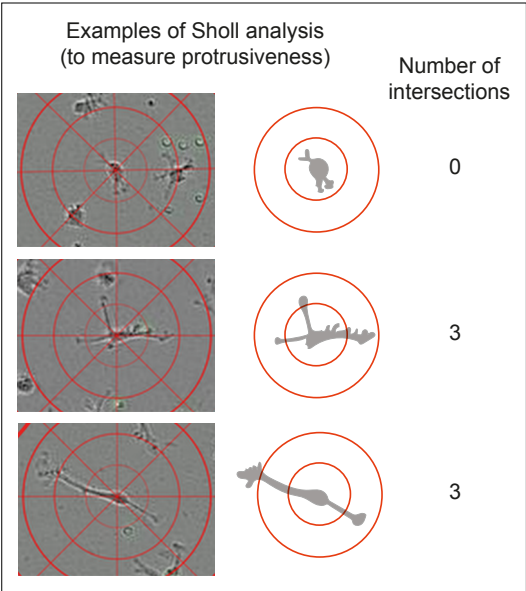


**Figure 5—figure supplement 2.** Measurement of cell protrusiveness by Sholl analysis (relates to **Figure 5F**). The center points of individual macrophages are overlaid with layers of concentric rings (Sholl cells) at 25  $\mu\text{m}$  intervals. The number of occasions Sholl shells are intersected by cellular process gives a measure of branch-based and elongation-based protrusiveness for an individual cell at a given timepoint.

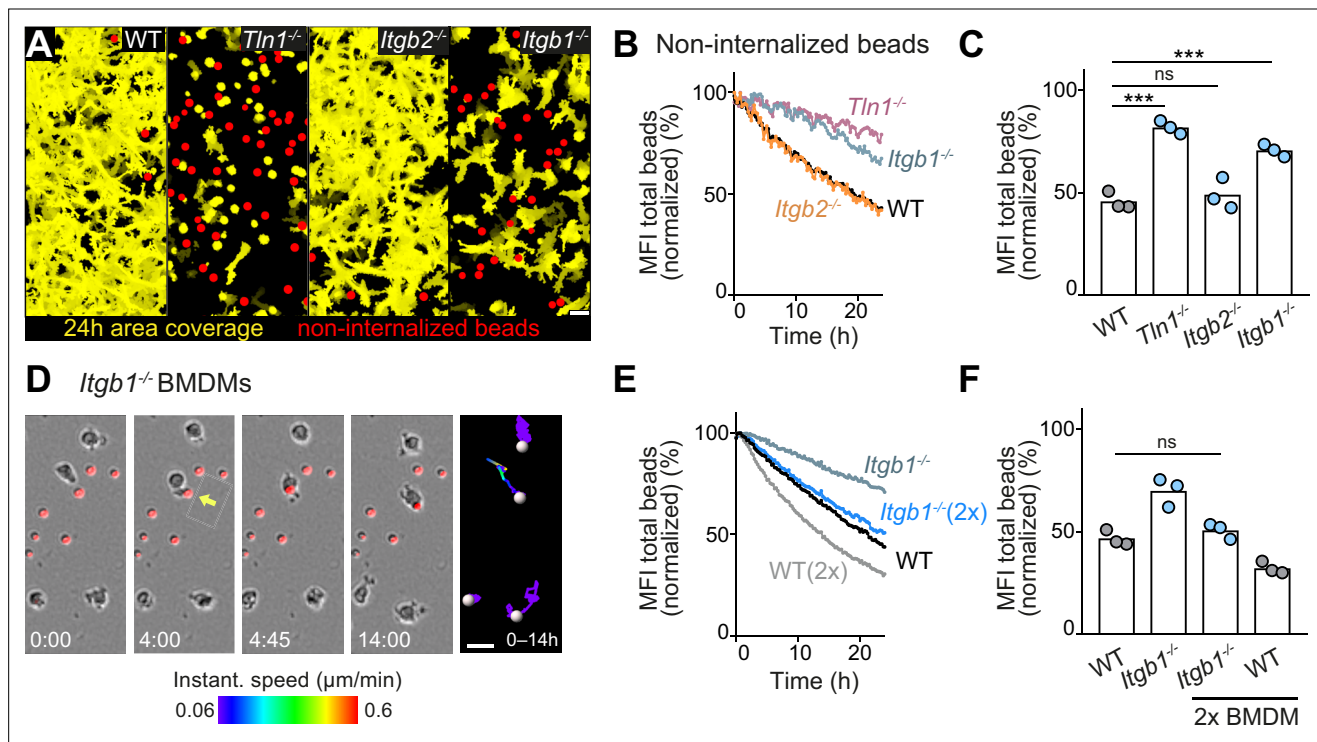


**Figure 6.** Haptokinesis is required for optimal bead removal by macrophage networks. (A–C) Analysis of bone marrow-derived macrophage (BMDM) network sampling activity upon genetic interference with integrin functionality was performed as described in Figure 5A–E. (D) Time sequence of an individual *Itgb1*<sup>-/-</sup> macrophage is shown, correlating bead sampling and migratory activity as described in Figure 5G and H. (E, F) Analysis of *Itgb1*<sup>-/-</sup> BMDM network sampling activity upon doubling (2x) the cell number in the BMDM network. Analysis of network sampling as described in Figure 5C–E. All bar graphs display the mean; \*\*\*p ≤ 0.001, ns: non-significant; Dunnett's multiple comparison (post hoc analysis of variance [ANOVA]). Scale bars: 40 μm (A), 20 μm (D).

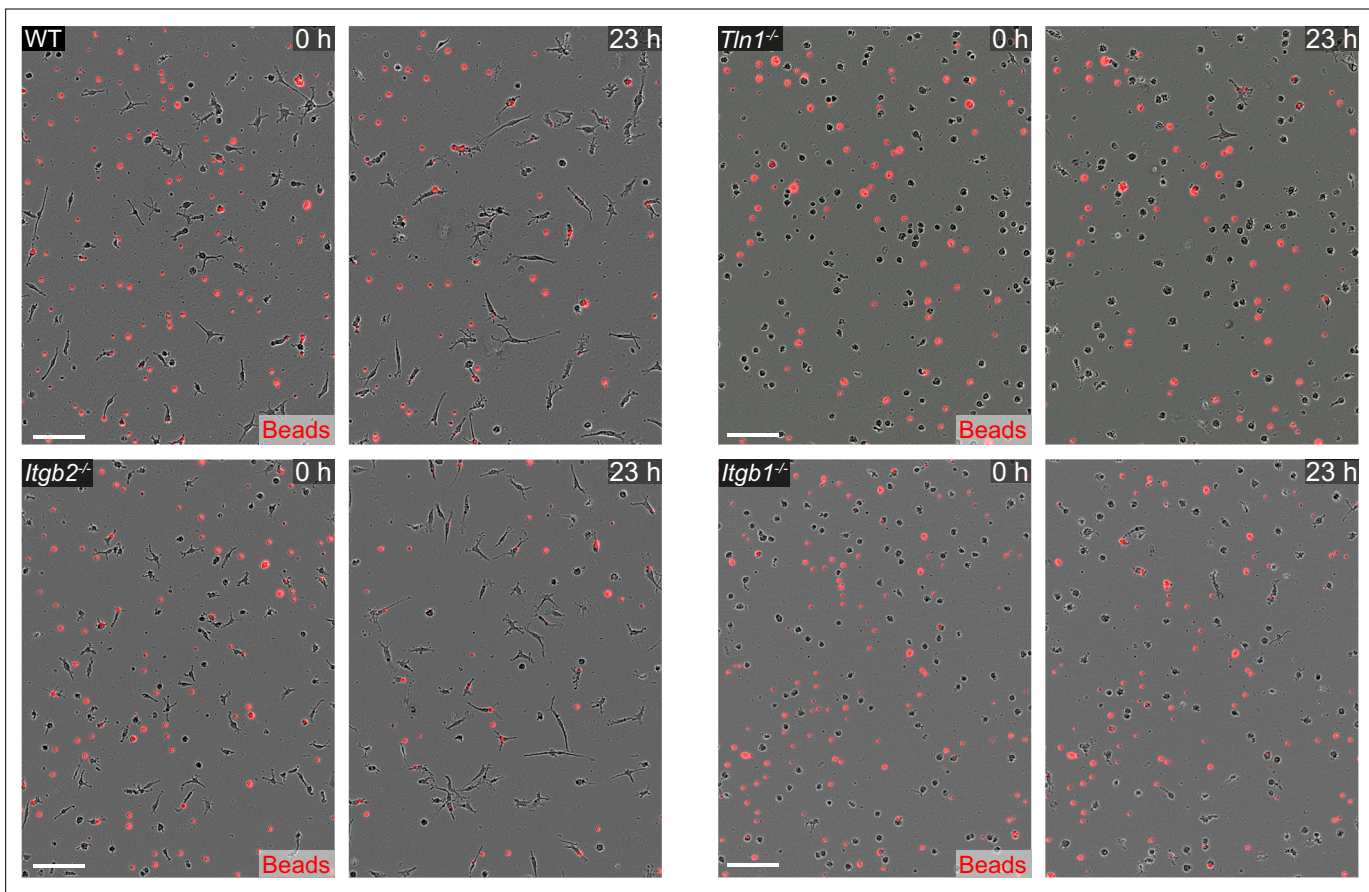


**Figure 6—figure supplement 1.** Macrophages require  $\beta 1$  integrins for migration-dependent bead removal in three-dimensional (3D) matrigel. Live-cell imaging snapshots showing the start (0 hr) and a late timepoint (23 hr) of bead removal by populations of WT, *Itgb1*<sup>-/-</sup>, *Itgb2*<sup>-/-</sup>, and *Tln1*<sup>-/-</sup> bone marrow-derived macrophages (BMDMs). WT and *Itgb2*<sup>-/-</sup> BMDMs move in 3D matrigel and reduce the number of extracellular beads, whereas migration-deficient *Tln1*<sup>-/-</sup> and *Itgb1*<sup>-/-</sup> BMDMs show impaired removal of extracellular beads. Extracellular, non-internalized fluorescent beads appear as bright red signal. Scale bars: 100  $\mu$ m.

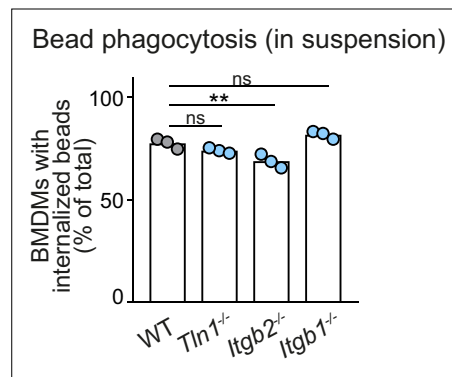


**Figure 6—figure supplement 2.** Macrophages do not require  $\beta 1$  integrins bead phagocytosis in suspension. Analysis of bead phagocytosis in cell suspensions. WT, *Itgb1*<sup>-/-</sup>, *Itgb2*<sup>-/-</sup>, and *Tln1*<sup>-/-</sup> bone marrow-derived macrophages (BMDMs) were kept in stirred cell suspensions with fluorescent beads for a 2 hr incubation time. Bead internalization by macrophages was quantified by flow cytometry analysis, using a combination of intrinsic bead fluorescence and an annexin V labelling of extracellular beads. Representative experiment with N = 3 technical replicates. Bars display the mean; ns: non-significant, \*\* $p \leq 0.01$ , Dunnett's multiple comparison (post hoc analysis of variance [ANOVA]).



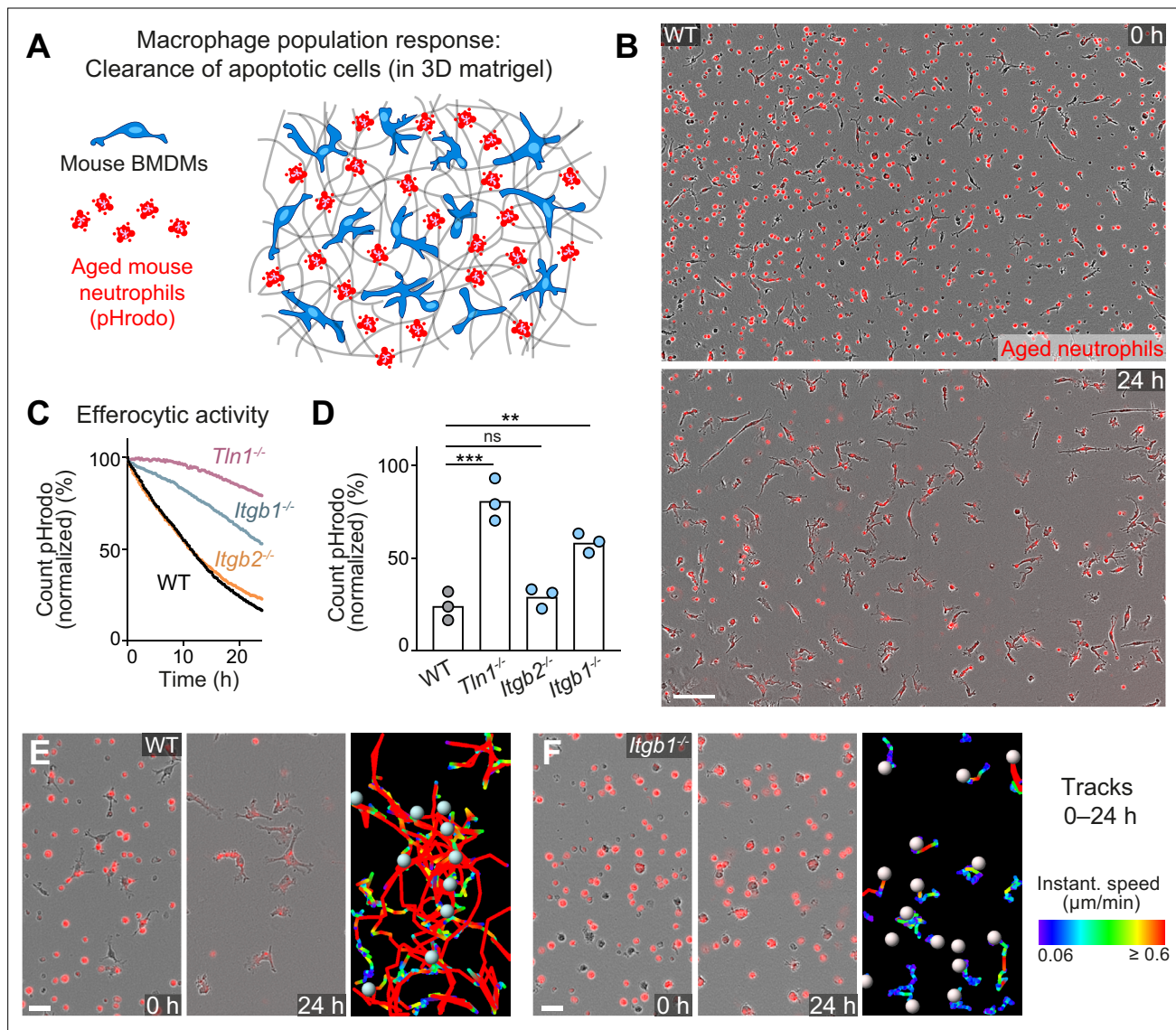


**Figure 7.** Haptokinesis is required for optimal efferocytosis by macrophage networks. **(A)** Scheme for studying the efferocytic response of macrophage networks in three-dimensional (3D) in vitro matrices. **(B)** Live-cell imaging snapshots showing the start (0 hr) and endpoint (24 hr) of dead cell clearance by a population of WT bone marrow-derived macrophages (BMDMs) (unstained). Extracellular, fluorescently pHrodo-labeled aged neutrophils (red, 0 hr) were engulfed and removed by BMDMs over time. The image shows a quarter of the total imaging field of view. Scale bar: 100 μm. **(C, D)** Analysis of dead neutrophil removal by BMDM networks upon genetic interference with integrin functionality. Neutrophil uptake and digestion by macrophages was measured as an object count decline of pHrodo in 15 min intervals over time, presented as **(C)** time-course analysis from one independent experiment (dots in curves are mean values from N = 2–5 technical replicates) (separate wells of matrigel), and as **(D)** 24 hr-mean-values calculated from three biological replicates (n = 3 per genotype). Bars display the mean; \*\*\*p ≤ 0.001, \*\*p ≤ 0.01, ns: non-significant; Dunnett's multiple comparison (post hoc analysis of variance [ANOVA]). **(E, F)** Correlation of efferocytic and migratory activity in populations of WT **(E)** and *Itgb1*<sup>-/-</sup> **(F)** BMDMs. Cell tracks over 24 hr are pseudo-colored for instantaneous speed values. Scale bars: 30 μm.

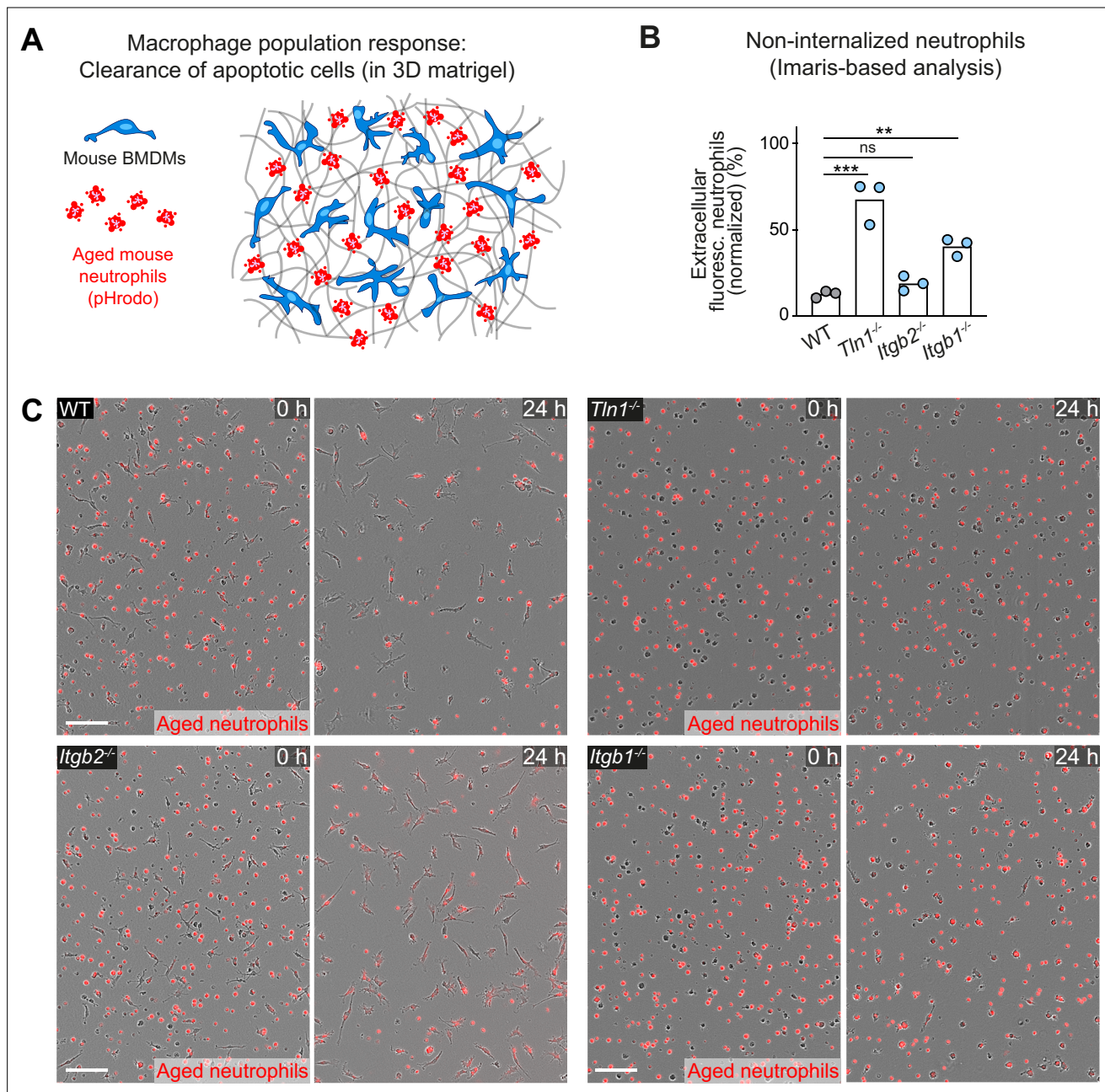


**Figure 7—figure supplement 1.** Haptokinetic sampling of dead cells optimizes efferocytosis in macrophage networks. **(A)** Scheme for studying the efferocytic response of macrophage networks in three-dimensional (3D) in vitro matrices (same as in **Figure 7A**). **(B)** Analysis of dead neutrophil removal after 24 hr by bone marrow-derived macrophage (BMDM) networks upon genetic interference with integrin functionality. Validation of our analysis based on the integrated software of the Incucyte live-cell imaging system (see **Figure 7D**). Imaris software-based analysis determined only the fluorescence signals of extracellular, non-internalized neutrophils 24 hr after start of the experiment. Neutrophil uptake is measured as an object count and displayed as normalized values of the initial neutrophil numbers (0 hr) for three independent experiments (N = 2–5 technical replicates, which means imaging wells with BMDMs and matrigel). Bars are mean; \*\*\* $p \leq 0.001$ , \*\* $p \leq 0.01$ , ns: non-significant; Dunnett's multiple comparison (post hoc analysis of variance [ANOVA]). **(C)** Live-cell imaging snapshots showing the start (0 hr) and endpoint (24 hr) of dead neutrophil (red) removal by populations of WT, *Itgb1*<sup>-/-</sup>, *Itgb2*<sup>-/-</sup>, and *Tln1*<sup>-/-</sup> BMDMs. Non-internalized dead neutrophils show bright red signal. Scale bars: 100  $\mu$ m.



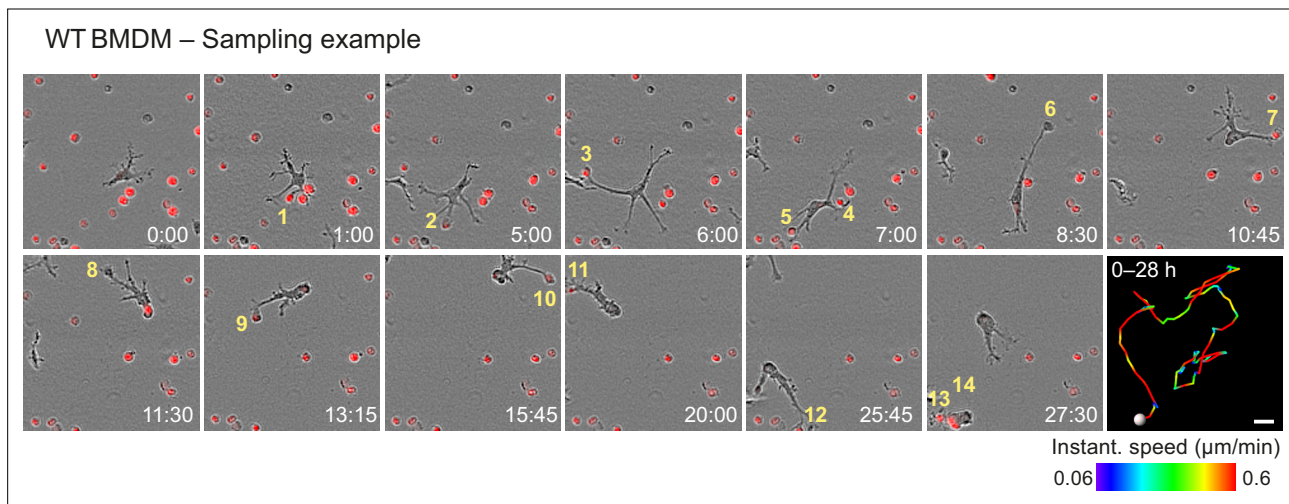


**Figure 7—figure supplement 2.** Haptokinetic sampling of dead cells optimizes efferocytosis in macrophage networks. Live-cell imaging and close-up view of an individual WT bone marrow-derived macrophage (BMDM) that samples and ingests several pHrodo-Red-labeled dead neutrophils over 28 hr. Yellow numbers indicate individual engulfed cell corpses. The cell track over 28 hr is pseudo-colored for instantaneous speed values. Scale bar: 20  $\mu\text{m}$ .

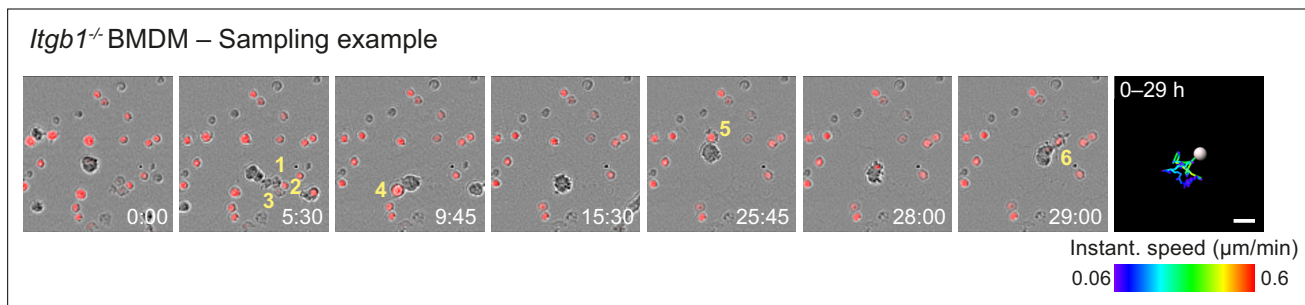


**Figure 7—figure supplement 3.** Haptokinetic sampling of dead cells optimizes efferocytosis in macrophage networks. Live-cell imaging and close-up view of an individual *Itgb1*<sup>-/-</sup> bone marrow-derived macrophage (BMDM) that samples and ingests several pHrodo-Red-labeled dead neutrophils over 29 hr. Yellow numbers indicate individual engulfed cell corpses. The cell track over 29 hr is pseudo-colored for instantaneous speed values. Scale bar: 20  $\mu\text{m}$ .

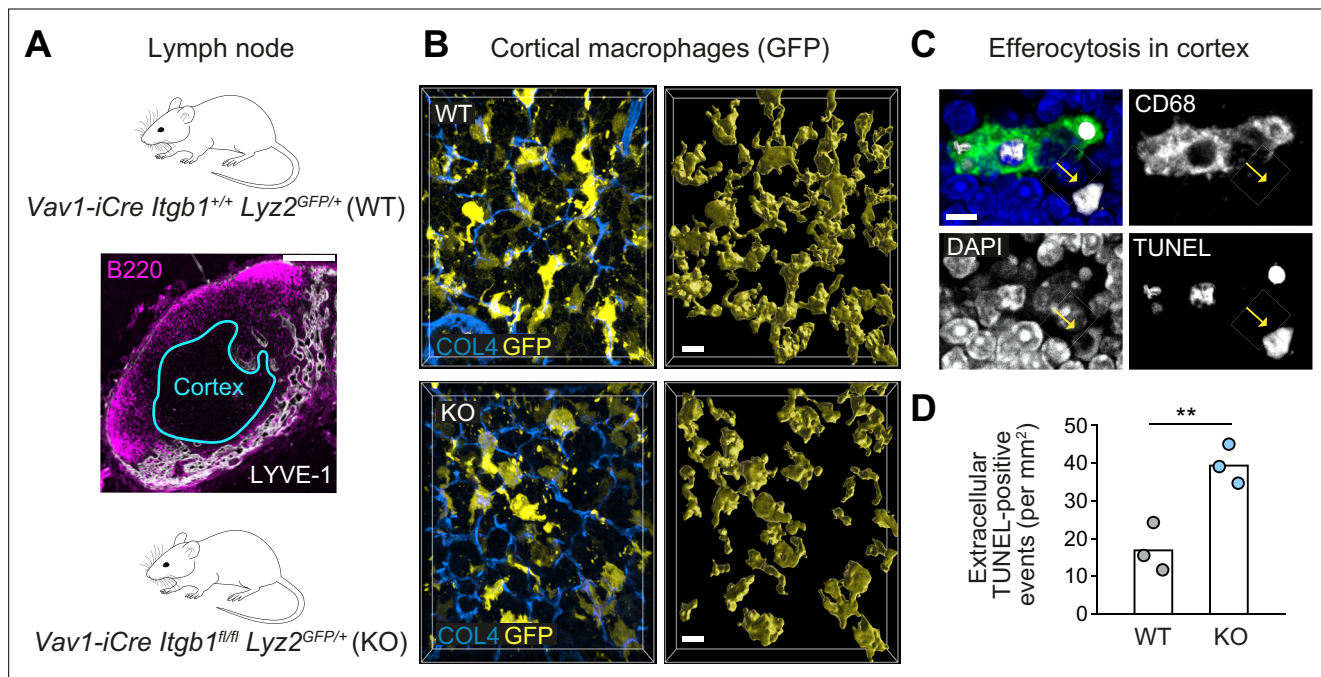


**Figure 8.**  $\beta$ 1 integrin-dependent surveillance by cortical macrophage networks in lymph nodes. **(A)** Immunofluorescence staining of a mouse inguinal lymph node. T cell cortex (cyan outline) was defined as B220- and Lyve-1-negative tissue area. **(B)** Confocal immunofluorescence images of GFP-expressing cortical macrophages in WT and conditional *Itgb1*-deficient mice crossed to *Lyz2<sup>GFP/+</sup>* knock-in mice (left). Collagen IV (COL4) stainings display the cortical reticular fiber network. GFP-based surface representations of macrophage morphologies are shown (right). **(C)** Detection of apoptotic cells by TUNEL method in T cell zones of immuno-stained lymph node sections. TUNEL-positive cells had altered nuclear DAPI stainings, and were found non-internalized (yellow arrow) or internalized by macrophages (stained by CD68). **(D)** Quantification of non-internalized TUNEL-positive cells in T cell cortices. Dots represent individual mice ( $n = 3$  per genotype). Bars display the mean; \*\* $p \leq 0.01$ ,  $t$  test. Scale bars: 100  $\mu$ m (**A**), 10  $\mu$ m (**B**), 5  $\mu$ m (**C**).